Flow, Turbulence and Combustion (2022) 109:991–1010
https://doi.org/10.1007/s10494-022-00355-5

Large Eddy Simulation of a Reacting Kerosene Spray in Hot Vitiated Cross-Flow

Daniel Fredrich[1] · Luigi Miniero[2] · Khushboo Pandey[2] · William P. Jones[1] · Nicolas Noiray[2] · Andrea Giusti[1]

Received: 23 March 2022 / Accepted: 25 July 2022 / Published online: 20 August 2022

Abstract

The evaporation and combustion characteristics of a kerosene spray injected perpendicularly into a cross-flow of high-temperature vitiated air is investigated. This fundamental flow configuration has wider implications for the future development of ultra-low emission aeronautical combustors, particularly with respect to technologies involving MILD combustion. Large eddy simulations with a Eulerian–Lagrangian framework are performed to investigate the spray evolution and the characteristics of the reaction zone for a range of conditions. For the closure of turbulence-chemistry interactions at the sub-grid scales, a transported probability density function approach solved by the Eulerian stochastic fields method is applied. A configuration based on the use of airblast atomisation is assessed first and compared with experimental observations. The effect of the atomiser air-to-liquid mass flow ratio is studied in greater detail, both in terms of the resulting gas-phase properties and the droplet evaporation process. Then, the effect of ambient pressure on the global spray flame behaviour is examined. For this part of the study, no atomising air is included in the simulation to separate the effects of ambient pressure on the spray from the interaction with the air jet. Analysis of the flame and spray properties at cross-flow operating pressures of 1 atm, 2 bar and 4 bar highlights the strong coupling between the reacting flow and droplet evaporation characteristics, which are highly affected by the penetration of the spray into a flow field characterised by relatively large gradients of temperature. The results reported in this work provide fundamental understanding for the development of novel low-emission combustion technologies and demonstrate the feasibility of applying large eddy simulation with detailed chemistry for the investigation of reacting aviation fuel sprays in hot vitiated cross-flow.

Keywords Air-blast atomisation · Spray flame · Jet A-1 fuel · MILD combustion · Clean aviation · LES-PDF

✉ Daniel Fredrich
d.fredrich15@imperial.ac.uk

[1] Department of Mechanical Engineering, Imperial College London, Exhibition Rd, London SW7 2AZ, UK

[2] CAPS Laboratory, Mechanical and Process Engineering Department, ETH Zürich, Sonneggstrasse 3, Zurich 8092, Switzerland

1 Introduction

The transverse injection of gaseous or liquid jets into a bulk cross-flow has been studied extensively in the past, see e.g., Karagozian (2010), and is commonly referred to as jet in cross-flow (JICF) or spray in cross-flow (SICF). Both JICF and SICF are characterised by enhanced mixing qualities in the near-field region of the two interacting streams and are therefore often utilised in technical applications. One such example is the fuel preparation process in aeronautical engines where rapid droplet evaporation and fuel-oxidiser mixing are desired to produce homogeneous mixtures with the aim of controlling the local air-to-fuel ratio and minimising the formation of pollutant emissions.

A specific case of reacting SICF is the injection of liquid fuel into a cross-flow of high-temperature vitiated air. The expression 'vitiated' (or 'diluted') air is used here to indicate a mixture of pure air and combustion products. At present, such configuration is only encountered in afterburner-type jet engines, where fuel can be temporarily injected into the bulk exhaust gas stream for increased thrust. However, in the near future, similar concepts involving the use of vitiated air may also be employed to further reduce the formation of pollutants in gas turbine engines (Perpignan et al. 2018), see e.g., the ultra-low emission aeronautical combustor concept recently proposed by de Oliveira et al. (2021). It was demonstrated in the past that the principle of oxidising fuel with heavily vitiated air offers the potential to decrease the production of nitrogen oxides (NO_X) during combustion (Wünning and Wünning 1997). In practice, this could be achieved for example by exhaust gas recirculation (EGR) or sequential combustor technologies (Schulz and Noiray 2019). The underlying concept is commonly known as moderate or intense low-oxygen dilution (MILD) combustion (Cavaliere and de Joannon 2004), or 'flameless' oxidation, and relies on the creation of small temperature gradients between the reactant mixture and the burnt products resulting in spatially well-distributed reaction zones.

Up to now, only a limited number of published works investigating spray combustion in vitiated air can be found in the open literature. Furthermore, previous studies of such conditions, both experimental and computational, have focused almost exclusively on co-flow and free-jet configurations. Only two prior works have targeted SICF configurations specifically, namely, the experimental work of Miniero et al. (2022) and the computational work of Brown et al. (2012). The former analysed the effect of the prescribed air-to-liquid mass-flow ratio (ALR) of an airblast (or air-assisted) atomiser. The complex flame structure was revealed via OH- and fuel-planar laser-induced fluorescence (PLIF) measurements for a stack of planes across the reactive region. This experimental configuration is investigated in the present work by means of numerical simulations (more details are provided below). The latter reports on the difficulties of simulating the transverse injection of Jet-A fuel into a vitiated cross-flow with an intermediate temperature of 1000 K. Results from several different computational fluid dynamics (CFD) simulations were compared to experimental measurements providing marginal agreement. Generally, the modelling of this highly complex flow problem is considered extremely challenging and requires advanced CFD tools with robust and accurate multiphase flow solvers, evaporation models and chemical reaction schemes. The difficulties arise from the wide variety of physical processes involved, i.e., the liquid fuel is injected in the form of a spray, which after vaporisation mixes with the excess oxygen contained in the high-temperature vitiated cross-flow and burns. Previous work on a gaseous jet in hot cross-flow also suggested auto-ignition as a fundamental mechanism

for flame stabilisation (Schulz et al. 2019), further demonstrating the importance of both the chemistry and flow time scales to determine the flame dynamics.

Large eddy simulation (LES) is the computational method applied in the present work, since it enables time-resolved, three-dimensional solutions to industrial-scale flow problems at a feasible computational cost. However, the use of LES introduces another dimension of complexity due to the need for a combustion model to close turbulence-chemistry interactions on the unresolved sub-grid scales. Various combustion models have been developed in the past, ranging from computationally less expensive methods such as flamelet generated manifolds (FGM) and artificially thickened flame models, to more expensive approaches like the conditional moment closure model or transported probability density function (PDF) methods. A comprehensive review of recent trends and developments in turbulent combustion modelling can be found in Giusti and Mastorakos (2019). Few research groups have previously published LES studies of spray flames in vitiated air. Examples are the works by Ma and Roekaerts (2016, 2017) and Gallot-Lavallée et al. (2017, 2021) who applied, respectively, the FGM method and the Eulerian stochastic fields method to the Delft spray in hot co-flow test case (Rodrigues et al. 2015). Overall, these studies demonstrate that numerical simulations are a mature tool for the prediction of spray combustion in vitiated air. Such studies also show that the spray boundary conditions and the modelling of the turbulence-chemistry interaction and evaporation effects are important for the prediction of the global characteristics of the flame.

The present work aims at extending the investigation of spray combustion in high-temperature (above 1800 K) vitiated air. To the best knowledge of the authors, this marks the first time in the open literature that an SICF is numerically simulated under such conditions. It should be noted that the quality of atomisation is an important aspect to be considered for any practical implementation of this configuration. When fuels with relatively low volatility such as kerosene are used, fine droplets are desired to achieve quick vaporisation. In a parallel experimental campaign by Miniero et al. (2022) it was found convenient to employ an airblast atomiser for this purpose. Experimental results also showed that the amount of air used for atomisation could affect the reaction zone. Therefore, the atomising air stream needs to be modelled carefully when numerical simulations of such a configuration are performed. The present work will provide more insight into the behaviour observed in the experiment through the application of LES.

The main objectives of the work are threefold: (i) to study the characteristics of the reaction zone of a spray in vitiated cross-flow when airblast atomisation with varying ALRs is utilised, (ii) to assess the impact of ambient pressure on the spray flame, and (iii) to demonstrate the feasibility of LES-PDF simulations of a turbulent reacting SICF in vitiated air conditions. To decouple the effects of pressure and ALR, the second objective is addressed by simulating injection without the additional air stream, which essentially corresponds to the use of a pressure atomiser. The applied transported PDF combustion model has the advantage of enabling a potentially burning regime-independent description of turbulent flames (further detailed in Sect. 2.2). It should also be noted that the investigated airblast configuration poses a three-stream problem due to the existence of two different oxidiser streams, i.e., the vitiated cross-flow and the pure air flow from the airblast atomiser. This makes combustion models based on variables involving the mixture fraction more difficult to use, as formulations suitable for multiple oxidiser streams—and hence multiple mixture fraction variables—need to be considered (Hasse and Peters 2005; Ihme and See 2011). The paper is organised as follows. First, the methodology is introduced followed by

a description of the numerical setup. Then, the results are presented and discussed. A summary and conclusions close the paper.

2 Methodology

2.1 Large Eddy Simulation

The LES method applied in this work is based on a Eulerian–Lagrangian framework with two-way coupling between the continuous (gas) and dispersed (liquid) phase of the flow. For the gas phase, Favre-filtered equations for mass conservation and momentum balance are solved under a variable density, low-Mach number approximation. These equations include source terms representing the influence of the liquid phase by assuming a dilute spray (Jenny et al. 2012):

$$\frac{\partial \overline{\rho}}{\partial t} + \frac{\partial \overline{\rho}\widetilde{u}_i}{\partial x_i} = \overline{\rho}\widetilde{\Pi} \tag{1}$$

$$\frac{\partial \overline{\rho}\widetilde{u}_i}{\partial t} + \frac{\partial \overline{\rho}\widetilde{u}_i\widetilde{u}_j}{\partial x_j} = -\frac{\partial \overline{p}}{\partial x_i} + \frac{\partial \overline{\tau}_{ij}}{\partial x_j} - \frac{\partial \tau_{ij}^{sgs}}{\partial x_j} + \overline{S}_{u,i} \tag{2}$$

where ρ denotes the density, t is the time, u_i and x_i are the velocity and spatial location in the ith direction, p is the pressure, and τ_{ij} is the viscous stress tensor. The source terms Π and S_u represent, respectively, the volumetric rate of phase change per unit volume and the transfer of momentum from the liquid to the gas phase. The sub-grid scale stress tensor τ_{ij}^{sgs} is closed by a dynamic version (Piomelli and Liu 1995) of the Smagorinsky model. The interaction between turbulence and chemistry on the unresolved sub-grid scales appears in the additional species transport equations (see e.g., Fredrich et al. (2021a)) in the form of a filtered chemical source term $\overline{\rho\dot{\omega}}_\alpha$, which requires modelling.

2.2 Eulerian Stochastic Fields Method

The combustion model utilised in this work is based on a modelled equation for the evolution of the joint filtered fine-grained PDF for the species mass fractions and mixture enthalpy. The main advantage of this formulation is that the chemical source terms appear in closed form allowing for a description of turbulent flames potentially independent of the burning regime. However, it is not feasible to numerically solve this equation directly due to the large number of independent variables involved. Instead, solution strategies based on either Lagrangian particle Monte Carlo methods or Eulerian stochastic field methods have been developed in the past. Both methods have been shown to provide similar results (Jaishree and Haworth 2012), however, the implementation of Eulerian field methods into conventional CFD codes is generally considered less difficult (Jones and Navarro-Martinez 2007). Moreover, in the specific case of LES, simpler mixing models and fewer samples usually suffice compared to Reynolds-averaged Navier-Stokes simulations, possibly making the advantages of particle-based methods less compelling (Jaishree and Haworth 2012).

A stochastic Eulerian field solution method (see e.g., Sabel'nikov and Soulard (2005)) is adopted in the present work, where the PDF evolution equation is statistically represented by an ensemble of $N = 8$ stochastic fields $\xi_\alpha^n(\mathbf{x}, t)$ corresponding to an equivalent system of stochastic differential equations:

$$\begin{aligned}\bar{\rho}\mathrm{d}\xi_\alpha^n + \bar{\rho}\widetilde{u}_i\frac{\partial\xi_\alpha^n}{\partial x_i}\mathrm{d}t = &\frac{\partial}{\partial x_i}\left[\left(\frac{\mu}{\sigma}+\frac{\mu_{sgs}}{\sigma_{sgs}}\right)\frac{\partial\xi_\alpha^n}{\partial x_i}\right]\mathrm{d}t - \bar{\rho}\frac{C_d}{2\tau_{sgs}}\left(\xi_\alpha^n - \widetilde{\phi}_\alpha\right)\mathrm{d}t \\ &+ \left(2\bar{\rho}\frac{\mu_{sgs}}{\sigma_{sgs}}\right)^{1/2}\frac{\partial\xi_\alpha^n}{\partial x_i}\mathrm{d}W_i^n + \overline{\rho}\dot{\omega}_\alpha^n(\underline{\xi}^n)\mathrm{d}t \\ &+ \overline{\rho}\left(\Pi_\alpha(\widetilde{\phi}_\alpha) - \Pi(\widetilde{\phi}_\alpha)\xi_\alpha^n\right)\mathrm{d}t\end{aligned} \tag{3}$$

with $1 \leqslant n \leqslant N$ and $1 \leqslant \alpha \leqslant N_s$; where N_s represents the number of scalars α, i.e., all species plus the enthalpy. μ and σ are, respectively, the viscosity and the Prandtl (or Schmidt) number, whereas μ_{sgs} and σ_{sgs} are their respective sub-grid scale quantities. A value of 0.7 is assigned to σ_{sgs}. The sub-grid scale micro-mixing term is approximated by the linear mean square estimation (LMSE) closure (Dopazo and O'Brien 1974) using a micro-mixing constant and time scale of $C_d = 2.0$ and $\tau_{sgs} = \overline{\rho}\Delta^2/\mu_{sgs}$, respectively. The Wiener process $\mathrm{d}W_i^n$ is different for each stochastic field but independent of the spatial location $\mathbf{x}$. $\mathrm{d}W_i^n$ is approximated by time-step increments defined as $\zeta_i^n(\mathrm{d}t)^{1/2}$ where ζ_i^n is a $\{-1, +1\}$ dichotomic random vector. The ensemble average over all stochastic fields finally yields the filtered mean value of each scalar quantity $\widetilde{\phi}_\alpha$. Note that this modelling approach has previously been applied to test cases involving premixed (Jones et al. 2012a), partially premixed (Fredrich et al. 2019, 2021b), non-premixed (Jones and Prasad 2010) and spray (Gallot-Lavallée et al. 2017, 2021) flames and does not require any tuning of the default model parameters.

2.3 Reaction Mechanisms

Two different reaction mechanisms for the modelling of vapour-phase kerosene-air combustion are employed in this work. In all simulations of the airblast atomisation setup (representing the experiment by Miniero et al. 2022), a comprehensive reaction mechanism involving 57 species is applied where dodecane ($C_{12}H_{26}$) is used as a single-component fuel surrogate for kerosene. The mechanism follows the work of Nehse et al. (1996) and enables the prediction of both oxidation and pyrolysis of the fuel, which are fundamental aspects for a more accurate comparison with the experiment. NO_X reaction kinetics based on the GRI-Mech 3.0 are also included.

As far as simulations with varying ambient pressure are concerned, a reduced 4-step mechanism is utilised. These simulations mainly focus on the relative location of the spray, fuel vapour and reacting regions. Although pyrolysis products are not included in the chemistry, the reduced mechanism still enables a reliable prediction of the flame location and, at the same time, considerably decreases the computational cost. The 4-step scheme was devised from a global reaction mechanism originally developed for alkanes (Jones and Lindstedt 1988) and includes 7 species (kerosene is represented by $C_{12}H_{23}$) with the following reaction steps:

$$H_2 + 0.5O_2 \rightleftharpoons H_2O \quad (R_1)$$
$$CO + H_2O \rightleftharpoons CO_2 + H_2 \quad (R_2)$$
$$C_{12}H_{23} + 12H_2O \rightharpoonup 12CO + 23.5H_2 \quad (R_3)$$
$$C_{12}H_{23} + 6O_2 \rightharpoonup 12CO + 11.5H_2 \quad (R_4)$$

The respective forward rate constants $\dot{r}_f$ were derived such that the measured burning velocities of gaseous kerosene-air mixtures are reproduced over a range of operating pressures, initial temperatures and mixture equivalence ratios:

$$\dot{r}_{f,1} = \frac{1.0 \times 10^{15}}{T} \exp\left(\frac{-40,000}{\mathcal{R}T}\right) \rho^{0.4} \sqrt{n_{H_2}} n_{O_2}^{1.9} / n_{H_2O}$$
$$\dot{r}_{f,2} = 2.75 \times 10^{9} \exp\left(\frac{-20,000}{\mathcal{R}T}\right) \rho n_{CO} n_{H_2O}$$
$$\dot{r}_{f,3} = 3.0 \times 10^{8} \exp\left(\frac{-30,000}{\mathcal{R}T}\right) \rho n_{C_{12}H_{23}} n_{H_2O}$$
$$\dot{r}_{f,4} = 8.5 \times 10^{9} \exp\left(\frac{-30,000}{\mathcal{R}T}\right) \rho^{0.4} \sqrt{n_{C_{12}H_{23}}} n_{O_2}^{0.9}$$

where n is the specific mole number of each species, T is the temperature and $\mathcal{R}$ is the universal gas constant. The reverse rates are obtained from the appropriate equilibrium constants based on the Gibbs free energy, which can be evaluated from thermodynamic data (Jones and Lindstedt 1988). A similar 4-step reaction scheme coupled with the Eulerian stochastic fields method was previously used in a number of LES studies (Jones and Tyliszczak 2010; Jones et al. 2012b, 2014) and provided promising results for the investigation of kerosene combustion in pure air.

The performance of the global 4-step mechanism in vitiated air conditions is assessed here against a detailed mechanism ('HyChem' (Wang et al. 2018; Xu et al. 2018)) involving a total of 843 reactions and 119 species. For this purpose, laminar diffusion flame simulations were performed providing a solution to the temperature and species concentrations in mixture fraction (η) space at constant scalar dissipation rates (SDR). More details on the approach used for the laminar diffusion flame simulations can be found in Paxton et al. (2019). The investigated conditions are equivalent to those found in the vitiated cross-flow (summarised in Table 1) and the fuel vapour is assumed to have a temperature of 475 K.

Figure 1 shows the temperature profile for a range of values of SDR. The results demonstrate that the 4-step mechanism is able to capture both the peak value of temperature and the flame behaviour around the stoichiometric region with reasonable accuracy. Some noticeable discrepancies, as also shown by the species profiles in Fig. 2, appear on the rich side of the flame, which can be attributed to the absence of a detailed description of the pyrolysis process. Note again that in the present work, the 4-step reaction mechanism is only applied to study the effect of ambient pressure on the spray evolution and global flame characteristics. It is also worth noting, as detailed in the next section, that in these simulations no atomising air is used (the injector represents a pressure atomiser configuration).

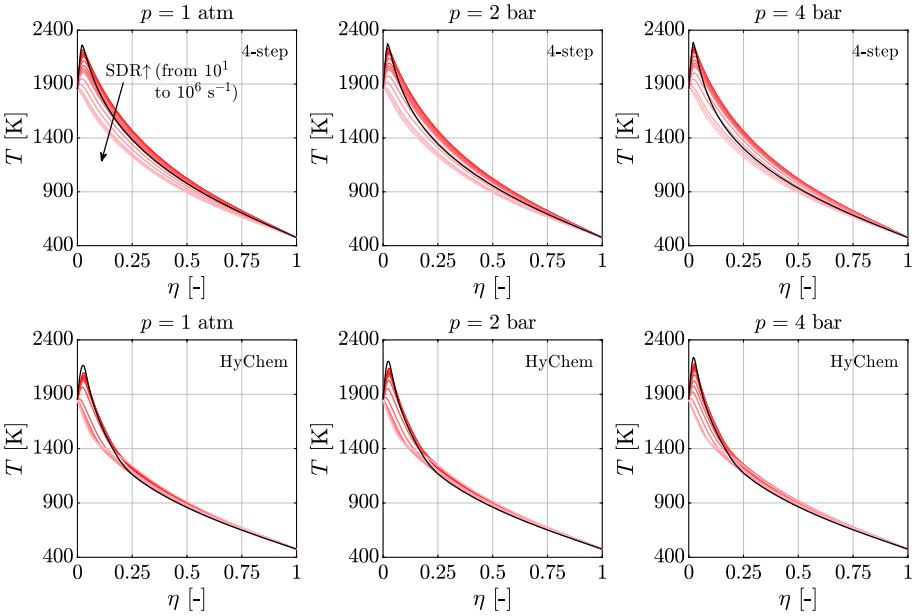

Fig. 1 Diffusion flame computations of the temperature T in mixture fraction space with the reduced 4-step (top) and more detailed 'HyChem' (bottom) reaction mechanisms at different pressures, $p = 1$ atm, 2 bar and 4 bar (from left to right). The scalar dissipation rate was gradually increased from 10 (black line) to 1×10^6 s^{-1}

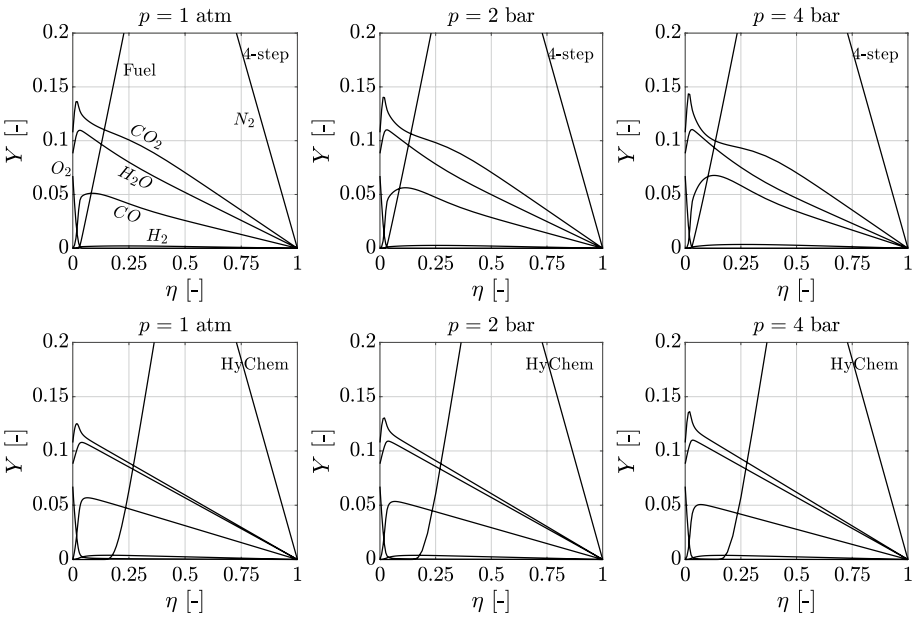

Fig. 2 Diffusion flame computations of the species mass fractions Y in mixture fraction space with the reduced 4-step (top) and more detailed 'HyChem' (bottom) reaction mechanisms at different pressures, $p = 1$ atm, 2 bar and 4 bar (from left to right), using a constant scalar dissipation rate of 100 s^{-1}

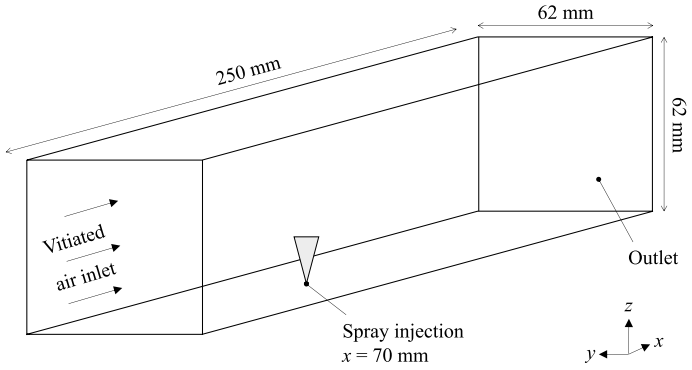

Fig. 3 Schematic of the simulated SICF geometry

Table 1 Cross-flow inlet temperature and composition

$\dot{m}_{cf}$ (g/s)	Φ_{cf} (–)	T_{cf} (K)	Y_{CO_2} (–)	Y_{H_2O} (–)	Y_{O_2} (–)	Y_{N_2} (–)
24.99	0.7	1850	0.108	0.088	0.065	0.739

3 Test Case

The investigated geometry is shown in Fig. 3 and consists of a 250 mm long duct with a 62×62 mm^2 square cross section area, which reproduces the experimental configuration studied by Miniero et al. (2022). The full domain is spatially discretised using a structured mesh of about 8 million hexahedral cells with uniform edge lengths of $\Delta_{x,y,z} = 0.5$ mm. Depending on the specific operating condition, a time-step of the order $\sim\mathcal{O}(10^{-7})$ is used to limit the Courant–Friedrichs–Lewy (CFL) number to a value of 0.3. In the corresponding experimental campaign (Miniero et al. 2022), a pre-burner was used to produce the cross-flow of vitiated air. The burner was supplied with a reactant mixture containing methane, hydrogen and air at ambient conditions using an equivalence ratio Φ_{cf} of 0.7 and a mass-flow rate $\dot{m}_{cf}$ of 24.99 g/s. The corresponding cross-flow temperature T_{cf} and composition to be used in the simulations were determined from an adiabatic equilibrium calculation. The resulting vitiated air conditions prescribed at the cross-flow inlet are summarised in Table 1. In accordance with experimental thermometry measurements, a non-uniform temperature profile is also imposed at the inlet along with a fully developed turbulent velocity profile based on the mean bulk velocity of the cross-flow U_{cf}. Approximate near-wall models (Hoffmann and Benocci 1995) are applied to describe the region between the walls and the nearest wall-adjacent grid point. Heat loss through the walls is taken into account via isothermal temperatures of 353 K at the bottom wall (injector location) and 973 K at the other three side walls. These temperatures are derived from measurements of the water-cooled bottom plate and experimental estimates, respectively (Miniero et al. 2022).

Two different injector configurations are applied in this study. The first one is representative of the airblast (A) atomiser setup utilised in the reference experiment (Miniero et al. 2022). In this configuration, pure air is injected around the fuel spray with a relatively high velocity to assist droplet atomisation. Therefore, in the simulation, an air inlet is included in correspondence of the droplet injection location. For the simulations with varying ambient pressure, droplets are injected without any additional air stream, therefore representing

Table 2 Overview of all operating conditions investigated in this work

Case	p_{cf} (bar)	$\dot{m}_f$ (g/s)	ALR (–)	ρ_{cf} (kg/m^3)	U_{cf} (m/s)	$U_{d,0}$ (m/s)	θ_s (°)	SMD (μm)
AI	1.01325	0.11	2	0.184	34.0	0.48	60	33.8
AII	1.01325	0.11	6	0.184	34.0	0.48	45	13.5
PI	1.01325	0.23	0	0.184	34.0	25.0	18	50
PII	2	0.23	0	0.364	17.2	17.8	18	50
PIII	4	0.23	0	0.728	8.6	12.6	18	50

a pressure (P) atomiser configuration. Table 2 summarises the different operating conditions investigated throughout this work. Cases AI and AII use the airblast atomiser setup with air-to-liquid mass-flow ratios of 2 and 6, respectively. Cases PI, PII and PIII represent the pressure atomiser setup with ambient cross-flow pressures p_{cf} of 1 atm, 2 bar and 4 bar. Note that both U_{cf} and the initial droplet injection velocity $U_{d,0}$ are adjusted at each ambient pressure such that the respective mass flow rates, overall equivalence ratio, Reynolds number, and spray-to-cross-flow momentum flux ratio ($J = \rho_{d,0}U_{d,0}^2/\rho_{cf}U_{cf}^2$, where $\rho_{d,0}$ and ρ_{cf} are the density of the liquid and cross-flow, respectively) are kept constant.

The fuel atomiser in all cases is located 70 mm downstream of the cross-flow inlet plane. The fuel droplets are injected in the form of a solid-cone spray with an opening angle θ_s and a temperature $T_{d,0}$ of 300 K. The initial droplet diameters d_0 are prescribed following a Rosin-Rammler distribution with a dispersion parameter q equal to 4. In the airblast configuration, the initial Sauter mean diameter (SMD) of the droplets as a function of ALR is estimated based on a well-established empirical formula (Rizk and Lefebvre 1984), which was validated experimentally by Chong and Hochgreb (2015). The initial droplet velocity is calculated from the fuel mass flow rate $\dot{m}_f$ and the area of the fuel injection orifice. An inflow of pure air at atmospheric pressure with a temperature of 300 K is used to model the transverse jet injected from the airblast atomiser. The jet velocity is calculated from the area of the air injection annulus and the respective ALR of each case. Droplet evaporation is evaluated with the rapid mixing model (Miller et al. 1998). Note that the diffusion properties of kerosene have been modified to reflect the influence of the ambient conditions on the evaporation rates. The modification is based on the findings derived from single droplet computations carried out by Fredrich and Giusti (2022). A stochastic dispersion model is included following the approach of Bini and Jones (2008). Drag is assumed to be the only force acting on the droplets and secondary breakup is neglected. All simulations are carried out with the in-house finite-volume LES code BOFFIN using second-order accurate schemes for the space discretisation and the Crank–Nicolson method for the time derivatives.

4 Results and Discussion

Results obtained with the two injection configurations (with and without air-assisted atomisation) are examined separately. The effect of atomising air on the flame and spray characteristics is discussed first. Comparisons with experiments are shown to assess the reliability of the numerical framework. This is followed by an analysis of the effect of ambient pressure on the evolution of the spray and the characteristics of the reacting region.

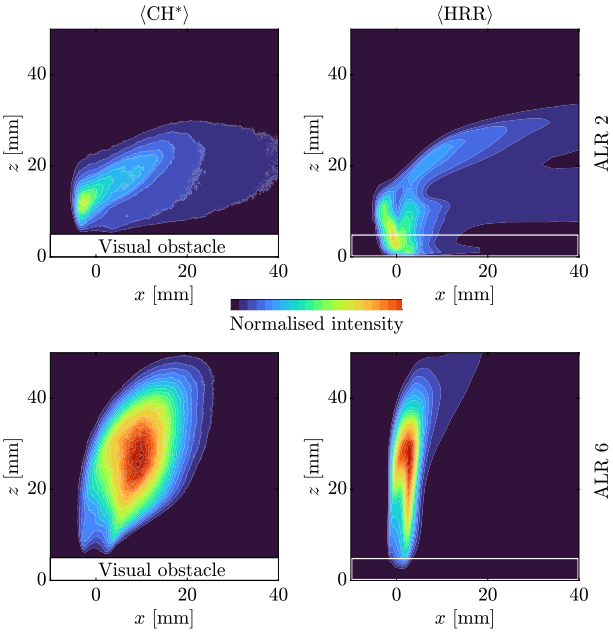

Fig. 4 Time-averaged CH* intensity from experimental measurements (left) and line-of-sight integration of the time-averaged heat release rate from the simulations (right) at ALR 2 (top) and ALR 6 (bottom). The respective colour maps are normalised by the maximum intensity across the two ALR cases

4.1 Effect of Atomising Air on the SICF

4.1.1 Reacting Flow Field

Figure 4 shows a comparison between the global flame topology observed at ALR 2 and ALR 6. The flame topology is visualised via CH* chemiluminescence images from experiments (Miniero et al. 2022) and the line-of-sight integrated heat release rate from the simulations. Care must be taken when comparing these two quantities since CH* chemiluminescence is not generally considered a reliable measure of heat release rate (Paul and Najm 1998), although it can help identify the location of the reacting region. The numerical and experimental results show qualitatively reasonable agreement with respect to the flame location and global flame structure, as well as on the variation of the flame structure with increasing ALR. For the case at ALR 6, the simulation reveals flame lift-off above the injector with a height of approximately 5 mm. A similar lift-off height may be inferred from the experimental image, however, this conjecture can not be verified due to the presence of a visual obstacle in the measurement setup. Upon increasing the ALR from 2 to 6, a shift of the location of the main reaction zone from the windward side of the jet to the leeward side is observed, which was first reported by Miniero et al. (2022). The exact reason for the relocation is not yet fully understood. A combination of effects is expected to play a role including differences in the initial droplet size distribution and the jet-to-cross-flow momentum flux ratio between the two ALRs. The former is expected to have a strong effect on the evaporation time scales, whereas the latter will affect important flow properties, such as the spray cone opening angle and the turbulence intensity. Hence, these parameters are further analysed in the following.

Figure 5 shows experimentally obtained (Miniero et al. 2022) single-shot images of the OH density measured in the mid-plane ($y = 0$ mm) at ALR 2 and ALR 6. A corresponding LES snapshot of the instantaneous OH mass fraction, along with several other gas-phase

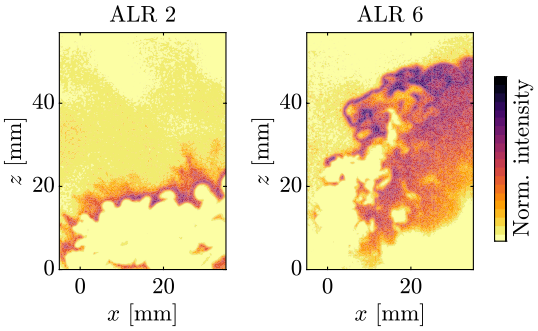

Fig. 5 Experimental single-shot images of the OH density in the mid-plane ($y = 0$ mm) at ALR 2 (left) and ALR 6 (right). The colour map is normalised by the maximum intensity across the two ALR cases

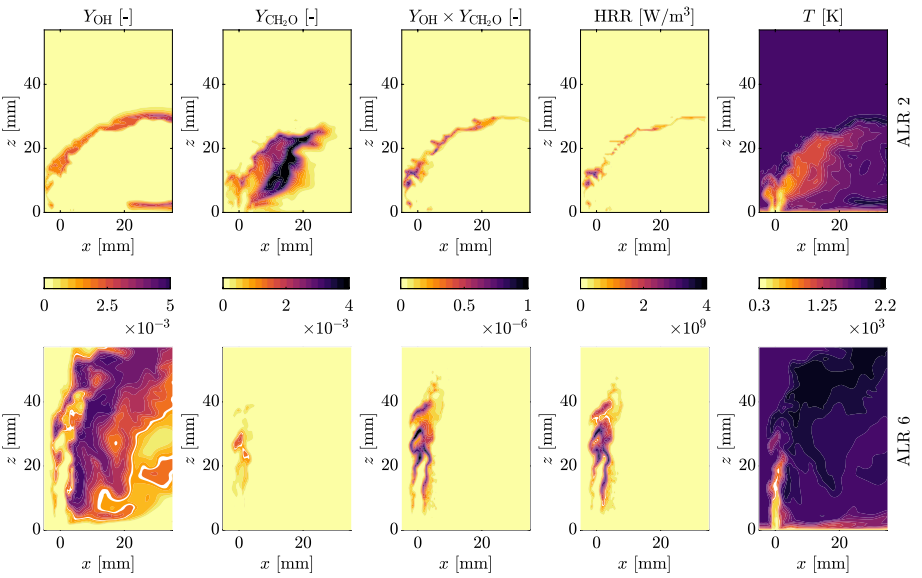

Fig. 6 Instantaneous scalar quantities in the mid-plane ($y = 0$ mm) at ALR 2 (top) and ALR 6 (bottom). From left to right: mass fractions of OH, CH_2O and their product, heat release rate and temperature

quantities, is shown in Fig. 6. It should be noted that a quantitative comparison between the measured OH density and the simulated OH mass fraction is not possible. Nonetheless, the predicted OH concentration is in qualitatively good agreement with the measurements. The LES captures the general flame structure including flame lift-off, which is caused by the absence of fuel vapour close to the injection location. As can also be deduced from Fig. 4, the bending of the jet trajectory is slightly under-predicted in the simulations leading to a marginally higher penetration of the cold reactants. Strong turbulence-induced flame wrinkling is shown in all images, with higher intensities observed at ALR 6. In the experimental images, some remnants of OH produced in the pre-burner can also be found in the cross-flow. However, due to the low concentration, these OH remnants are not accounted for in the cross-flow composition prescribed in the LES.

Comparison of the heat release rate and the product of OH and formaldehyde (CH_2O) indicates that the latter provides an excellent experimental marker for the location of maximum heat release. This correlation was initially validated by Paul and Najm (1998) for

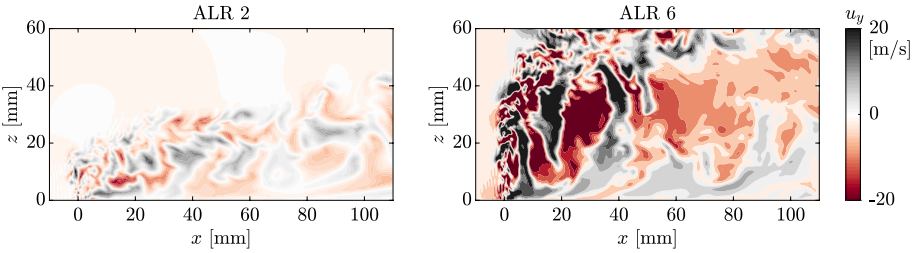

Fig. 7 Instantaneous transverse velocity component in the mid-plane ($y = 0$ mm) at ALR 2 (left) and ALR 6 (right)

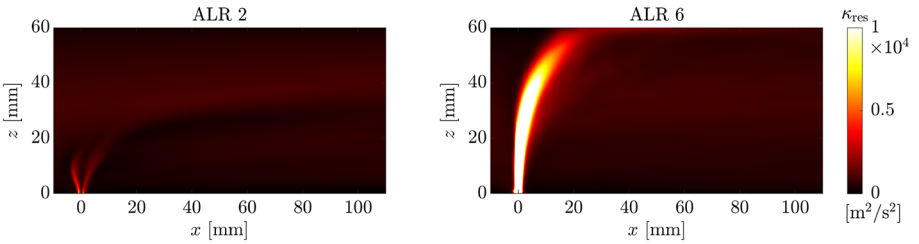

Fig. 8 Time-averaged resolved turbulence kinetic energy κ_{res} in the mid-plane ($y = 0$ mm) at ALR 2 (left) and ALR 6 (right)

laminar premixed flames. It was later shown that despite certain drawbacks, the product of Y_{OH} and Y_{CH_2O} is also a good indicator for increased chemical activity in multi-component fuels (Nikolaou and Swaminathan 2014). More recently, the correlation was extended to non-premixed flames at elevated pressures (Paxton et al. 2019) and to the case of a premixed gaseous jet in hot vitiated cross-flow (Schulz et al. 2019). The present work confirms that $Y_{OH} \times Y_{CH_2O}$ may also be used to identify the topology of a kerosene spray flame in high-temperature vitiated air conditions.

Snapshots of the instantaneous temperature suggest a weak correlation between the region of maximum temperature and OH concentration in close proximity to the reaction layers. In the case of ALR 2, the temperature results show that the low-temperature region is wider and penetrates less high into the cross-flow. This is a consequence of the wider cone angle of the spray and the lower mass flow rate and momentum of the atomising air. Hence, at ALR 2, evaporation is completed closer to the injection location, leading to the formation of a fuel-rich region that extends on the leeward side of the jet. This region shows negligible amounts of OH and strong peaks of CH_2O. Pyrolysis products are thus formed and oxidation is completed further downstream in a region with relatively low turbulence (not shown here). Conversely, in the case of ALR 6, the higher penetration of the fuel into the cross-flow ensures faster mixing with the vitiated air stream. The mixture on the leeward side of the spray is globally lean, leading to an increase of the temperature in this area ($0 < x < 20$ mm) compared to the ALR 2 case.

Snapshots of the instantaneous transverse velocity component and the time-averaged resolved turbulence kinetic energy are shown in Figs. 7 and 8, respectively. These results indicate higher levels of turbulence in the case of ALR 6, which are induced by the increased air mass flow rate and therefore higher jet velocity of the atomising air stream. It should be noted here that the atomising air only has a marginal effect on the global

equivalence ratio of the present test case. The maximum resolved turbulence kinetic energy is almost one order of magnitude higher at ALR 6, suggesting enhanced mixing between the fuel, airblast air and vitiated air streams. At ALR 2, small amounts of unburnt hydrocarbons (UHCs) are still detected at the domain outlet 180 mm downstream of the injector. To get an estimate of the evolution of these UHCs along the duct length, the mass flow rates of CH_2O, C_2H_4, C_4H_8 and $C_{12}H_{26}$ were quantified in several axial planes as shown in Fig. 9. Significant amounts of formaldehyde (cf. Fig. 6) and C_2H_4 underline the importance of fuel pyrolysis, especially at ALR 2, and justify the utilisation of detailed chemistry in the simulations. Overall, a relatively higher concentration of UHCs are found downstream of the injector at ALR 2 compared to ALR 6. This is an indicator of poor fuel penetration and mixing, and could result in incomplete combustion and low combustion efficiencies in practical combustor applications. Higher ALRs should therefore generally be considered to enhance the mixing quality between the fuel vapour and the two oxidiser streams.

In addition to improved combustion efficiencies, the use of higher ALRs could also lead to reduced pollutant emissions. When switching from ALR 2 to ALR 6, the integrated CO and NO_X emissions in the outlet plane decrease from approximately 3200 ppm to 230 ppm and from 14 to 10 ppm, respectively. The remarkably high level of CO at ALR 2 can partly be explained by incomplete combustion (derived from the results in Fig. 9), which on the other hand, may also limit the magnitude of the computed NO_X emissions. The overall reduction of both pollutants at ALR 6 is a result of three main effects. First, by creating a more homogeneous fuel-air mixture, the formation of fuel-rich pockets causing local peaks in the NO_X formation can be mitigated. Second, enhanced mixing with the vitiated air stream will lead to preheating of the cold reactants, thereby reducing the temperature gradient between the reactants and products. This may create locally favourable conditions for the transition to a MILD-type combustion regime (Miniero et al. 2022). Third, the increased air jet velocity at higher ALR induces a more efficient atomisation process with smaller droplet size distributions, which accelerates the droplet evaporation time scales. A more detailed discussion of the effects of ALR on droplet evaporation is presented next.

4.1.2 Spray Evolution

A slice through the instantaneous droplet cloud at ALR 2 and ALR 6 is presented in Fig. 10. Only droplets located within a distance of 0.5 mm from the mid-plane ($y = 0$ mm) are shown. The resulting spatial distribution of droplets is coloured by the instantaneous age, diameter and temperature of each droplet. Consistent with the afore-mentioned gas-phase observations, a higher vertical droplet penetration is achieved at ALR 6. It is also

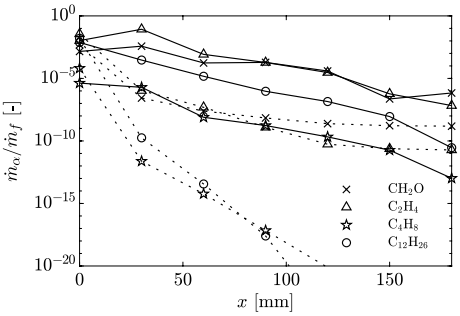

Fig. 9 Streamwise evolution of the mass flow rates of different gaseous species $\dot{m}_\alpha$ normalised by the total liquid fuel mass flow rate at ALR 2 (solid lines) and ALR 6 (dashed lines)

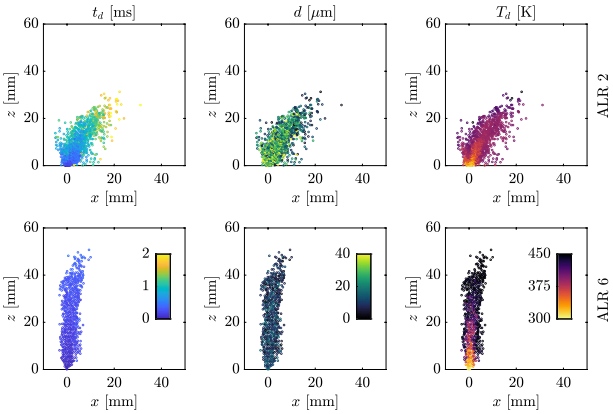

Fig. 10 Instantaneous spatial droplet distribution in the mid-plane ($y = \pm 0.5$ mm) coloured by, respectively, the droplet age, diameter and temperature (from left to right) at ALR 2 (top) and ALR 6 (bottom)

clear that the location of the droplet cloud mostly coincides with the location of the cold air jet injected from the atomiser. This is due to the relatively low inertia of the droplets, which tend to follow the surrounding air jet (low Stokes number). The air jet therefore acts as protective layer, shielding the droplets from the hot vitiated air stream. This allows the evaporation process to take place within a confined low-temperature core followed by turbulent mixing between the fuel vapour and the two oxidiser streams. As also reported in the experiments (Miniero et al. 2022), the larger droplet size distribution, increased spray cone opening angle and lower air mass flow rate in the case of ALR 2 may cause larger droplets with higher inertia to escape the cold air jet before complete evaporation. Although not directly modelled in the simulations, once these droplets reach the vitiated cross-flow, diffusion flames at the droplet level could develop (Fredrich and Giusti 2022), which tend to promote the formation of pollutants.

To further quantify the different spray properties at ALR 2 and ALR 6, normalised PDF distributions of the droplet age, diameter, temperature and velocity components in all three directions are shown in Fig. 11. At ALR 6, the high-velocity air jet injected from the atomiser appears to be very effective in transferring momentum to the droplets. Smaller average droplet sizes (consistent with the specified initial droplet size distributions) and shorter droplet residence times compared to ALR 2 are also evident. A bi-modal behaviour in the temperature distribution is obtained in both cases, showing a low-temperature peak that represents droplets surrounded by the cold air jet and a high-temperature peak indicating droplets that have reached equilibrium closer to the flame brush. Such bi-modal behaviour is also observed (to a greater degree) in the simulations without atomising air discussed in Sect. 4.2.2. Overall, these results confirm the afore-mentioned trend towards higher vertical droplet penetration and quicker evaporation with increasing ALR and are consistent with the characteristics of the reacting flow field.

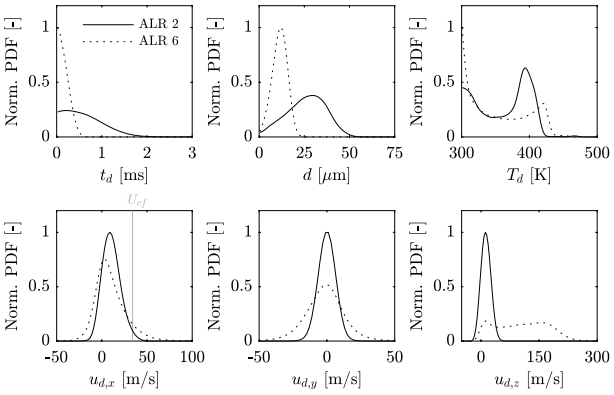

Fig. 11 Normalised PDF distributions of the droplet age, diameter, temperature and velocity components at ALR 2 and ALR 6

4.2 Effect of Ambient Pressure on the SICF

4.2.1 Reacting Flow Field

Simulations with no atomising air (i.e., the pressure atomiser setup) are used to analyse the effect of increasing the ambient operating pressure of the cross-flow. Figure 12 shows snapshots of the time-averaged temperature in the mid-plane ($y = 0$ mm) for the three investigated ambient pressures of 1 atm, 2 bar and 4 bar. The location of the reacting region is similar for all pressures. As expected, the thickness of the reaction zone appears to become thinner with higher pressure. Interestingly, the extension of the low-temperature region in the vicinity of the injection location decreases with increasing pressure. This is mainly caused by a decrease of the evaporation time scale at high pressure, further demonstrated in Fig. 13, which shows that the penetration of the spray increases with increasing pressure. The two main effects responsible for the increased spray penetration are discussed in the following.

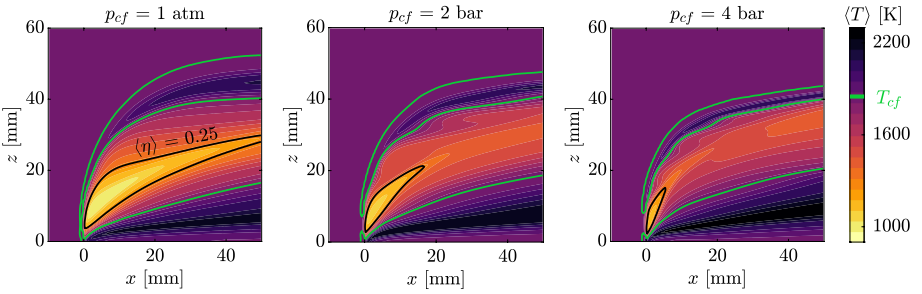

Fig. 12 Time-averaged temperature in the mid-plane ($y = 0$ mm) at ambient operating pressures of 1 atm, 2 bar and 4 bar (from left to right). Green and black lines indicate isocontours of the time-averaged temperature equal to T_{cf} (1850 K) and the time-averaged mixture fraction equal to 0.25, respectively

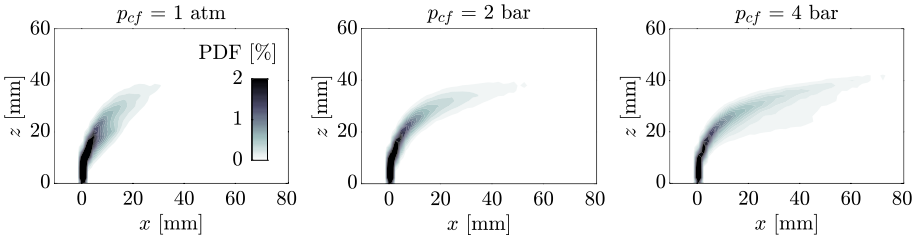

Fig. 13 PDF of the spatial droplet distribution (2D projection) at p_{cf} = 1 atm, 2 bar and 4 bar. The sample space is decomposed into a grid of 2×2 mm^2 cells

4.2.2 Spray Evolution

To gain further insight into the evaporation behaviour of the kerosene droplets, single droplet simulations in quiescent air at atmospheric and elevated pressure were performed using the method reported in Giusti et al. (2017). Figure 14 shows the time evolution of the normalised droplet diameter d^2/d_0^2 and the droplet temperature T_d. The total evaporation time increases with increasing pressure mainly as a result of an increase of the droplet heat-up period (Fredrich and Giusti 2022). Note that the maximum temperature a droplet can reach at equilibrium also increases with increasing pressure due to a higher vapour pressure at the droplet surface.

Considering again the SICF investigated here, the evaporation rate at high pressure is further affected by the characteristics of the cross-flow. In order to maintain a constant spray-to-cross-flow momentum flux ratio, both the cross-flow velocity and the initial droplet velocity had to be adjusted at higher ambient pressure (see Table 2). This leads to differences in the relative velocity between the droplets and the bulk flow, which directly affects the droplet Reynolds number Re_d and therefore the evaporation rates. The instantaneous distribution of Re_d along with the respective relative velocities is shown in Fig. 15; quantifying the trend towards lower mean droplet Reynolds numbers with increasing pressure. The lower Re_d is directly correlated to slower evaporation rates, thus contributing to the afore-mentioned higher spray penetration and longer droplet lifetimes (cf. Fig. 16) at elevated pressure.

Normalised PDF distributions of the droplet age, diameter, temperature and velocity components in all three directions are shown in Fig. 16 for each ambient pressure. In accordance with the observations mentioned above, the results demonstrate that the residence time of the droplets inside the domain increases with increasing pressure. The droplet temperature PDF appears bi-modal in all investigated cases (similar to the cases with airblast atomisation). The bi-modal shape could be representative of a quick transition from

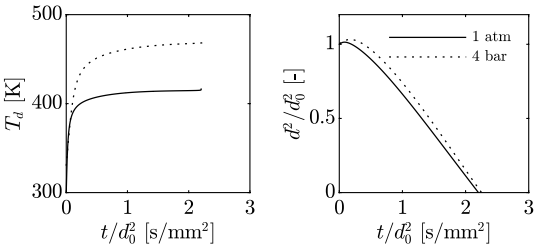

Fig. 14 Time evolution of the temperature (left) and the normalised droplet diameter (right) from 1D simulations of a single droplet (d_0 = 50 μm, $T_{d,0}$ = 300 K) in quiescent air with an ambient temperature of 1500 K and pressures of 1 atm and 4 bar

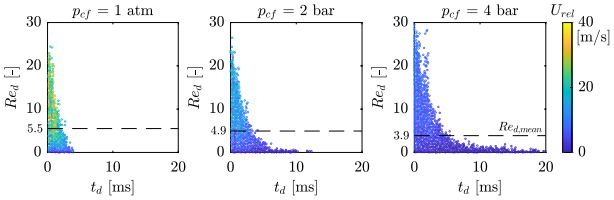

Fig. 15 Instantaneous distribution of the droplet Reynolds number coloured by the relative velocity U_{rel} between the droplets and the bulk flow at $p_{cf} = 1$ atm, 2 bar and 4 bar. Dashed lines indicate the mean droplet Reynolds number across all droplets

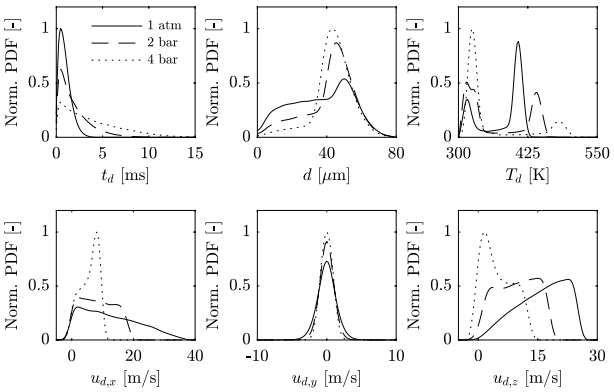

Fig. 16 Normalised PDF distributions of the droplet age, diameter, temperature and velocity components at $p_{cf} = 1$ atm, 2 bar and 4 bar

an equilibrium temperature in a relatively low-temperature region of droplets surrounded by fuel vapour to a higher equilibrium temperature of droplets that penetrate closer to the reaction zone. The relative number of droplets reaching high-temperature equilibrium is higher at low pressures. It is also evident that the maximum droplet temperature increases with pressure, which is consistent with the single droplet investigation presented in Fig. 14.

5 Summary and Conclusions

Large eddy simulations were performed to study the characteristics of a turbulent reacting kerosene spray injected perpendicularly into a cross-flow of high-temperature vitiated air. The applied LES method is based on a Eulerian–Lagrangian formulation and utilises the Eulerian stochastic fields method for the closure of sub-grid scale turbulence-chemistry interactions. A comprehensive reaction mechanism including 57 species, as well as a reduced 4-step reaction mechanism were employed for the investigation of test cases involving airblast and pressure atomisation, respectively. The performance of the 4-step mechanism in vitiated air conditions was first assessed via laminar diffusion flame simulations in mixture fraction space. Comparison against a detailed mechanism demonstrated reasonable accuracy around the stoichiometric flame region.

Simulations of the airblast atomiser setup, which was also studied in a parallel experimental campaign, were performed with varying air-to-liquid mass flow ratios. It was found that by varying the ALR of the atomiser, significant changes in the spray flame behaviour can be observed. By increasing the ALR from 2 to 6, a relocation of the main reaction zone from the windward side of the jet to the leeward side was identified. This relocation

is mainly a function of the droplet size distribution and the jet-to-cross-flow momentum flux ratio induced by the airblast stream underlining the strong coupling between droplet evaporation and the reacting flow. The influence of elevated cross-flow operating pressures on the spray flame characteristics was also studied. For this purpose, simulations with no atomising air were performed to decouple the effects of ambient pressure and ALR. Results showed that the main effect of increasing the ambient pressure is to delay droplet evaporation due to the combined effects of a longer droplet heat-up period, which increases with increasing pressure, and a decrease of the relative velocity between the droplets and the surrounding gas. This led to an increased downstream penetration of the spray with a subsequent impact on the global flame topology. The reported findings may support the development of low-emission aeronautical combustor technologies based on MILD combustion principles. In addition, the feasibility of applying LES with a state-of-the-art PDF combustion model and detailed chemistry to the simulation of spray combustion in vitiated air conditions was successfully demonstrated.

Funding The authors kindly acknowledge the UKCTRF for providing computational time on the ARCHER UK National Supercomputing Service (http://www.archer.ac.uk) under Grant No EP/R029369/1. This project has received funding from the Clean Sky 2 Joint Undertaking (JU) under Grant Agreement No 831804. The JU receives support from the European Union's Horizon 2020 research and innovation programme and the Clean Sky 2 JU members other than the Union.

Declaration

Conflict of interest The authors declare that they have no conflict of interest.

References

Bini, M., Jones, W.: Large-eddy simulation of particle-laden turbulent flows. J. Fluid Mech. **614**, 207–252 (2008)

Brown, C., Mondragon, U., McDonell, V., Kiel, B.: Comparison of CFD predictions and experimental measurements of liquid jet injection into a vitiated crossflow. In: 48th AIAA/ASME/SAE/ASEE Joint Propulsion Conference & Exhibit, p. 4327 (2012)

Cavaliere, A., de Joannon, M.: Mild combustion. Prog. Energy Combust. Sci. **30**(4), 329–366 (2004)

Chong, C.T., Hochgreb, S.: Effect of atomizing air flow on spray atomization of an internal-mix twin-fluid atomizer. At. Sprays **25**(8), 657–673 (2015)
de Oliveira, P.M., Fredrich, D., De Falco, G., El Helou, I., D'Anna, A., Giusti, A., Mastorakos, E.: Soot-free low-NOx aeronautical combustor concept: the lean azimuthal flame for kerosene sprays. Energy Fuels **35**(9), 7092–7106 (2021)
Dopazo, C., O'Brien, E.E.: Functional formulation of nonisothermal turbulent reactive flows. Phys. Fluids **17**(11), 1968–1975 (1974)
Fredrich, D., Giusti, A.: Numerical investigation of multi-component droplet evaporation and autoignition for aero-engine applications. Combust. Flame **241**, 112023 (2022)
Fredrich, D., Jones, W., Marquis, A.J.: The stochastic fields method applied to a partially premixed swirl flame with wall heat transfer. Combust. Flame **205**, 446–456 (2019)
Fredrich, D., Jones, W.P., Marquis, A.J.: Thermo-acoustic instabilities in the PRECCINSTA combustor investigated using a compressible LES-pdf approach. Flow Turbul. Combust. **106**(4), 1399–1415 (2021a)
Fredrich, D., Jones, W., Marquis, A.: A combined oscillation cycle involving self-excited thermo-acoustic and hydrodynamic instability mechanisms. Phys. Fluids **33**(8), 085122 (2021b)
Gallot-Lavallée, S., Jones, W., Marquis, A.: Large eddy simulation of an ethanol spray flame under MILD combustion with the stochastic fields method. Proc. Combust. Inst. **36**(2), 2577–2584 (2017)
Gallot-Lavallée, S., Jones, W., Marquis, A.: Large eddy simulation of an ethanol spray flame with secondary droplet breakup. Flow Turbul. Combust. **107**(3), 709–743 (2021)
Giusti, A., Mastorakos, E.: Turbulent combustion modelling and experiments: recent trends and developments. Flow Turbul. Combust. **103**(4), 847–869 (2019)
Giusti, A., Sidey, J.A.M., Borghesi, G., Mastorakos, E.: Simulations of droplet combustion under gas turbine conditions. Combust. Flame **184**, 101–116 (2017)
Hasse, C., Peters, N.: A two mixture fraction flamelet model applied to split injections in a di diesel engine. Proc. Combust. Inst. **30**(2), 2755–2762 (2005)
Hoffmann, G., Benocci, C.: Approximate wall boundary conditions for large eddy simulations. In: Advances in Turbulence V, pp. 222–228. Springer, Dordrecht (1995)
Ihme, M., See, Y.C.: Les flamelet modeling of a three-stream mild combustor: analysis of flame sensitivity to scalar inflow conditions. Proc. Combust. Inst. **33**(1), 1309–1317 (2011)
Jaishree, J., Haworth, D.: Comparisons of Lagrangian and Eulerian pdf methods in simulations of non-premixed turbulent jet flames with moderate-to-strong turbulence-chemistry interactions. Combust. Theor. Model. **16**(3), 435–463 (2012)
Jenny, P., Roekaerts, D., Beishuizen, N.: Modeling of turbulent dilute spray combustion. Prog. Energy Combust. Sci. **38**(6), 846–887 (2012)
Jones, W., Lindstedt, R.: Global reaction schemes for hydrocarbon combustion. Combust. Flame **73**(3), 233–249 (1988)
Jones, W., Navarro-Martinez, S.: Large eddy simulation of autoignition with a subgrid probability density function method. Combust. Flame **150**(3), 170–187 (2007)
Jones, W., Prasad, V.: Large eddy simulation of the Sandia flame series (D-F) using the Eulerian stochastic field method. Combust. Flame **157**(9), 1621–1636 (2010)
Jones, W.P., Tyliszczak, A.: Large eddy simulation of spark ignition in a gas turbine combustor. Flow Turbul. Combust. **85**(3), 711–734 (2010)
Jones, W., Marquis, A., Prasad, V.: LES of a turbulent premixed swirl burner using the Eulerian stochastic field method. Combust. Flame **159**(10), 3079–3095 (2012a)
Jones, W., Lyra, S., Navarro-Martinez, S.: Numerical investigation of swirling kerosene spray flames using large eddy simulation. Combust. Flame **159**(4), 1539–1561 (2012b)
Jones, W., Marquis, A., Vogiatzaki, K.: Large-eddy simulation of spray combustion in a gas turbine combustor. Combust. Flame **161**(1), 222–239 (2014)
Karagozian, A.R.: Transverse jets and their control. Prog. Energy Combust. Sci. **36**(5), 531–553 (2010)
Ma, L., Roekaerts, D.: Modeling of spray jet flame under MILD condition with non-adiabatic FGM and a new conditional droplet injection model. Combust. Flame **165**, 402–423 (2016)
Ma, L., Roekaerts, D.: Numerical study of the multi-flame structure in spray combustion. Proc. Combust. Inst. **36**(2), 2603–2613 (2017)
Miller, R.S., Harstad, K., Bellan, J.: Evaluation of equilibrium and non-equilibrium evaporation models for many-droplet gas-liquid flow simulations. Int. J. Multiph. Flow **24**(6), 1025–1055 (1998)
Miniero, L., Pandey, K., Shcherbanev, S., Doll, U., Noiray, N.: Tomographic reconstruction of oh density maps for Jet-A1 spray flame in a vitiated crossflow. In: AIAA SCITECH 2022 Forum, p. 1873 (2022)

Nehse, M., Warnatz, J., Chevalier, C.: Kinetic modeling of the oxidation of large aliphatic hydrocarbons. Symp. (Int.) Combust. **26**(1), 773–780 (1996)
Nikolaou, Z.M., Swaminathan, N.: Heat release rate markers for premixed combustion. Combust. Flame **161**(12), 3073–3084 (2014)
Paul, P.H., Najm, H.N.: Planar laser-induced fluorescence imaging of flame heat release rate. Symp. (Int.) Combust. **27**(1), 43–50 (1998)
Paxton, L., Giusti, A., Mastorakos, E., Egolfopoulos, F.N.: Assessment of experimental observables for local extinction through unsteady laminar flame calculations. Combust. Flame **207**, 196–204 (2019)
Perpignan, A.A., Rao, A.G., Roekaerts, D.J.: Flameless combustion and its potential towards gas turbines. Prog. Energy Combust. Sci. **69**, 28–62 (2018)
Piomelli, U., Liu, J.: Large-eddy simulation of rotating channel flows using a localized dynamic model. Phys. Fluids **7**(4), 839–848 (1995)
Rizk, N., Lefebvre, A.: Spray characteristics of plain-jet airblast atomizers. J. Eng. Gas Turbines Power **106**(3), 634–638 (1984)
Rodrigues, H.C., Tummers, M.J., van Veen, E.H., Roekaerts, D.J.: Spray flame structure in conventional and hot-diluted combustion regime. Combust. Flame **162**(3), 759–773 (2015)
Sabel'nikov, V., Soulard, O.: Rapidly decorrelating velocity-field model as a tool for solving one-point Fokker–Planck equations for probability density functions of turbulent reactive scalars. Phys. Rev. E **72**(1), 016301 (2005)
Schulz, O., Noiray, N.: Combustion regimes in sequential combustors: flame propagation and autoignition at elevated temperature and pressure. Combust. Flame **205**, 253–268 (2019)
Schulz, O., Piccoli, E., Felden, A., Staffelbach, G., Noiray, N.: Autoignition-cascade in the windward mixing layer of a premixed jet in hot vitiated crossflow. Combust. Flame **201**, 215–233 (2019)
Wang, H., Xu, R., Wang, K., Bowman, C.T., Hanson, R.K., Davidson, D.F., Brezinsky, K., Egolfopoulos, F.N.: A physics-based approach to modeling real-fuel combustion chemistry-I. Evidence from experiments, and thermodynamic, chemical kinetic and statistical considerations. Combust. Flame **193**, 502–519 (2018)
Wünning, J., Wünning, J.: Flameless oxidation to reduce thermal NO-formation. Prog. Energy Combust. Sci. **23**(1), 81–94 (1997)
Xu, R., Wang, K., Banerjee, S., Shao, J., Parise, T., Zhu, Y., Wang, S., Movaghar, A., Lee, D.J., Zhao, R., et al.: A physics-based approach to modeling real-fuel combustion chemistry–II. Reaction kinetic models of jet and rocket fuels. Combust. Flame **193**, 520–537 (2018)